Ltd. This flume was equipped with a piston-type wave generator with a maximum stroke of 2.0 m to enable the generation of tsunamis and an active wave absorption system to prevent the re-reflection of waves.

Figures 1 and 2 show a schematic of an experimental setup. An impermeable bed with a trench filled with sand (median grain size: 0.17 mm) was set inside the flume, and a coastal dike composed of a sand core (median grain size: 0.17 mm) covered with fluid-tight acrylic plates was constructed on the sand bed. It should be noted that the acrylic plates was fixed on the side walls of the flume because this study focused on the mechanism of local scouring at the landward toe of the dike. To measure water surface fluctuation, three capacitance-type wave gauges (Kenek Co.) were placed at W1, W6 (5.0 m offshore from the seaward toe of the dike), and W3.

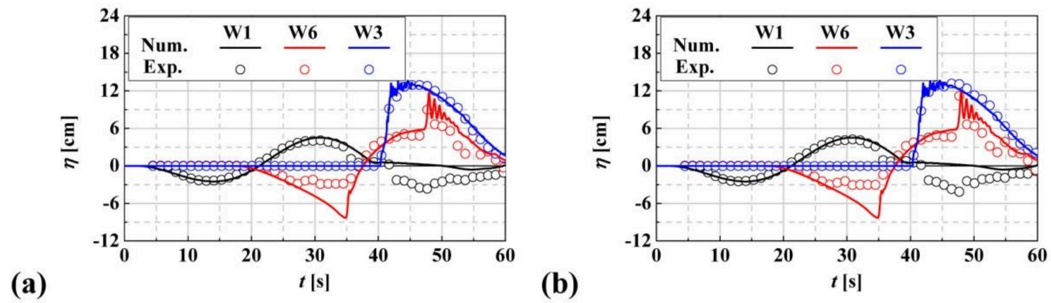

Figure 4. Comparison of the water surface fluctuation η for (a) the landward slope of 1/2 and (b) the landward slope of 1/1.

The still water depth h was set at the same height as the impermeable bed, i.e., h = 0.76 m, and a leading-depression long-period wave with a period of 40 s was generated toward the dike. Under this wave condition, the landward slope of the dike was changed to 1/2 and 1/1, as shown in Figure 2. In total, two experimental cases were conducted. After each experimental run, the surface profile of the sand bed was measured using a laser displacement sensor (Keyence Co.).

NUMERICAL SIMULATIONS

The numerical simulations were carried out applying the FS3M to the hydraulic experiments mentioned above.

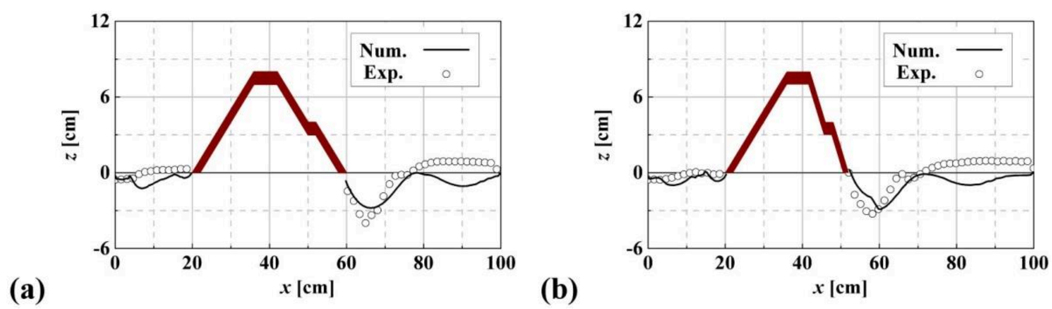

Figure 5. Comparison of the final surface profile of the sand bed for (a) the landward slope of 1/2 and (b) the landward slope of 1/1.

For the fluid analysis employing the main solver, the VOF module, and the ST module, we used the computational domain of Figure 3, which was modeled from the experimental setup. It should be noted that the IB module was not employed because the acrylic plates covering the sand core of the dike was not movable.

In preliminary simulations, it was confirmed that the size of the numerical cells had a little effect on numerical results in terms of water surface fluctuation and final scour profiles. Accordingly, the following size of the numerical cells was selected to ensure an appropriate balance with computational effort: uniform cells of 5.0 ×2.5 mm for the vicinity of the surface of the sand bed, i.e., $0.0 \leq x \leq 1.0$ m and $-0.05 \leq z \leq 0.03$ m, those of 5.0 ×2.5 mm for its upper and lower regions, i.e., $0.0 \leq x \leq 1.0$ m and $-0.10 \leq z \leq -0.05$ m, and $0.0 \leq x \leq 1.0$ m and $0.03 \leq z \leq 0.10$ m, and nonuniform cells with increasing width in each direction for the remainder of the entire domain.

For the main solver and the VOF module, the water level and flow velocity were specified at the offshore boundary so that the water surface fluctuation at W1 matched with experimental data as possible. At the other boundaries, the following conditions were used for flow velocity and pressure: the slip condition for the surfaces of the bottom, the impermeable bed, and the acrylic plates; the gradient-free condition for the onshore boundary; and the constant-pressure condition for the top boundary. For these boundaries, we also imposed the gradient-free condition for the VOF function. In the ST module, it was assumed that no bed-load sediment was supplied from the seaward and landward edges of the sand bed, and no suspended sediment was supplied from the offshore and onshore boundaries.

As for the model parameters of the ST module, the density and porosity of the sand bed were assumed to be 2.65×10^3 kg/m^3 and 0.40 because of the lack of experimental data. For the same reason, the static friction angle θ_s, the kinematic friction angle θ_d, the angle of repose θ_r, the criterion for starting sand slide θ_r^+, and the criterion for ending sand slide θ_r^- were also unavailable. The value of θ_r was assumed to be 42.00° according to the maximum angle of the final surface profile of the sand bed measured in the hydraulic experiments. For simplicity, the value of $\theta_r + \theta_r^+$ was assumed to be equal to that of θ_r, i.e., $\theta_r^+ = 0.00°$, and the value of $\theta_r - \theta_r^-$ was assumed to be slightly smaller than that of θ_r, i.e., $\theta_r^- = 0.01°$. From preliminary simulations using these parameters under the condition of $\theta_d \leq \theta_r - \theta_r^- \leq \theta_r \leq \theta_r + \theta_r^+ \leq \theta_s$, we determined $\theta_d = 27.00°$ and $\theta_s = 42.01°$. For the model parameters of the main solver, see Nakamura and Yim (2011).

For the coupled soil-water analysis using the FE module, the vicinity of the surface of the sand bed near the landward toe of the dike was discretized with uniform isoparametric brick elements with a dimension of 10 mm, and the remainder of the sand bed was discretized with non-uniform isoparametric brick elements. The fixed support and undrained condition was used for the bottom of the sand bed, and the roller support and undrained condition was used for the lateral boundaries. For the sand bed, the shear modules of elasticity and the Poisson ratio were assumed to be 1.00×10^8 N/m^2 and 0.33, and the hydraulic conductivity was estimated to be 3.13 $\times10^{-5}$ m/s using the Kozeny-Carman equation (Bear, 1972). For the acrylic plates, the density, the shear modules of elasticity, and the Poisson ratio were set at the values of acrylic, i.e., 1.19×10^3 kg/m^3, 1.16×10^9 N/m^2, and 0.35. The apparent bulk modulus of water was set at 2.20×10^5 N/m^2 to take into account small amount of air in pore water.

PREDICTIVE CAPABILITY OF NUMERICAL MODEL

Figure 4 shows a comparison of water surface fluctuation η. As shown in Figure 4, the second backwash at W1 is underestimated because the active wave absorption system has been used in the hydraulic experiments. Furthermore, the first backwash at W6 is underestimated because the wave gauge has been installed slightly away from the bottom in the hydraulic experiments. However, the changes in η are predicted well regardless of the landward slope of the dike.

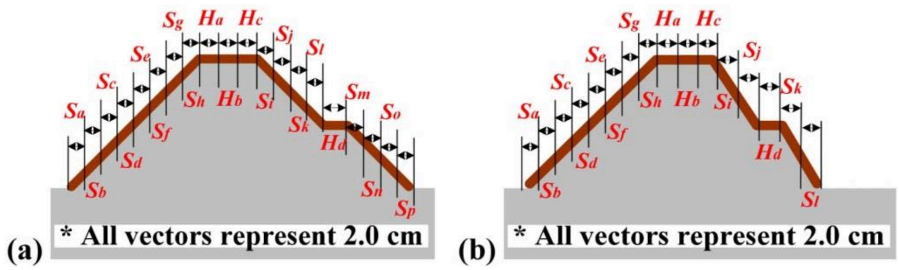

Figure 6. Location of the armor blocks for (a) the landward slope of 1/2 and (b) the landward slope of 1/1.

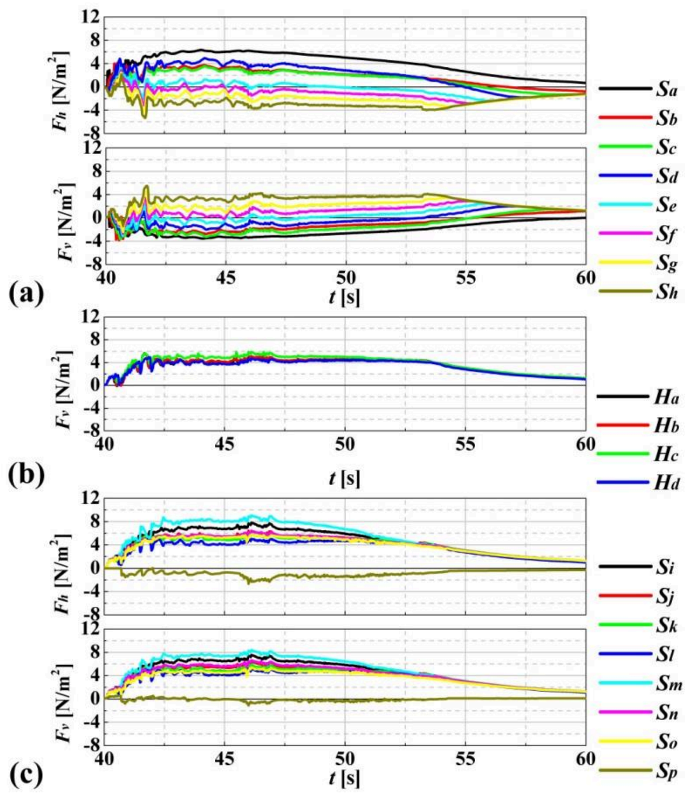

Figure 7. Horizontal force F_h and the vertical force F_v on each segment of (a) the seaward slope (S_a – S_h), (b) the crown (H_a – H_c) and the berm (H_d), and (c) the landward slope (S_i – S_p) for the landward slope of 1/2.

Figure 5 shows a comparison of the surface profile of the sand bed after the tsunami overflow. From Figure 5, it is observed that deposition is formed around the landward edge of the sand bed in the hydraulic experiments, while the sand bed at the same position is eroded in the numerical simulations. From video images recorded in the hydraulic experiments and snapshots obtained from the numerical simulations, it was confirmed that hydraulic jump was formed above the scour hole in both cases. However, the hydraulic jump in the numerical simulations was formed more slowly than the hydraulic experiments. During this delay period, the sand bed continued to be eroded in the numerical simulations. This led to the different trend around the landward edge of the sand bed. However, Figure 5 indicates a reasonably well correlation between the experimental data and the numerical results in terms of the width and depth of the scour hole at the landward toe of the dike.

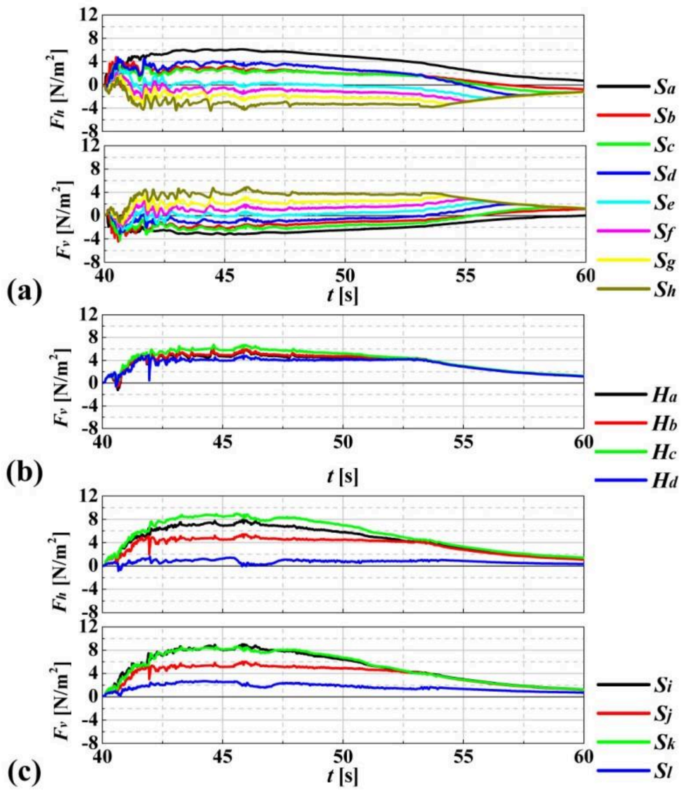

Figure 8. Horizontal force H_h and the vertical force F_v on each segment of (a) the seaward slope (S_a – S_h); (b) the crown (H_a – H_c) and the berm (H_d), and (c) the landward slope (S_i – S_l) for the landward slope of 1/1.

From these results, the predictive capability of the FS3M was demonstrated in terms of the water surface fluctuation and the profile of the scour hole.

STABILITY OF ARMOR BLOCKS

As illustrated in Figure 6, the acrylic plates are divided into segments with a horizontal length of 20 mm, and each segment is called S_a to S_h for the seaward side, H_a to H_c for the crown, H_d for the berm, S_i to S_p and S_i to S_l for the landward side with the slopes of 1/2 and 1/1. This section focuses on horizontal force F_h and vertical force F_v per unit area acting on each segment. Here, F_h is defined as positive landward, and F_v is defined as positive upward.

Figures 7 and 8 show the temporal changes in F_h and F_v on each segment.

At the seaward side, Figures 7(a) and 8(a) indicate that the value of F_h decreases and that of F_v increases with approaching the crown, and large seaward and upward force acts on the segment at the top of the slope (S_h). Figure 9 shows the distribution of pressure P during the tsunami overflow. From this figure, it is observed that high pore-air pressure builds inside the dike. Consequently, as mentioned above, the seaward and upward force acts on the segment at S_h.

At the crown and the berm, as shown in Figures 7(b) and 8(b), all segments receive upward force because of the high pore-air pressure inside the dike. Furthermore, the upward force on the most landward segment (H_c) is slightly larger than that on the other segments. This is because water pressure around the top of the landward slope decreases due to the separation of flow, as shown in Figure 9.

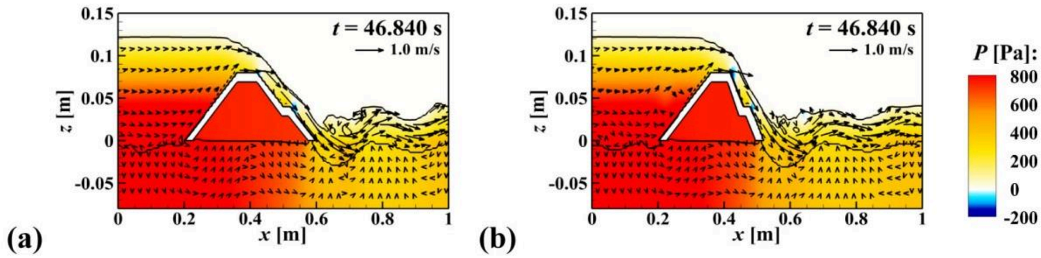

Figure 9. Distribution of the pressure *P* for (a) the landward slope of 1/2 and (b) the landward slope of 1/1.

At the landward side, Figures 7(c) and 8(c) indicate that the values of F_h and F_v increase with approaching the crown and the berm from the bottom, and large landward and upward force acts on the segments below the crown and the berm (*Si* and S_m for the landward slope of 1/2, S_i and S_k for the landward slope of 1/1). This is due to the increase in the pore-air pressure inside the dike and the decrease in the water pressure induced by the flow separation. Moreover, the vertical force F_v on the segments below the crown and the berm for the landward slope of 1/1 (S_i, S_k) is slightly larger than that for the landward slope of 1/2 (S_i, S_m). This is because, as pointed out by Kotake and Isobe (2012), the scale of the flow separation and the resulting decrease in the water pressure are larger for the landward slope of 1/1.

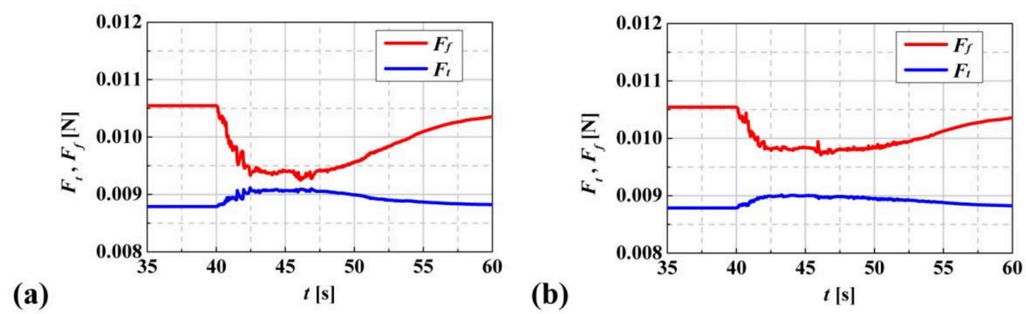

Figure 10. Tangential force F_t and the maximum static friction force F_f on the blocks (a) below the berm (S_m) and (b) between the berm and the toe (S_o) for the landward slope of 1/2.

To evaluate the stability of armor blocks, 2 t blocks are assumed to be placed below the berm (S_m) and between the berm and the toe (S_o) for the landward slope of 1/2. Here, the dimension and weight of the blocks are 13.2×13.2×5.0 mm and 2 g in the experimental scale. Figure 10 shows the temporal changes in tangential force F_t and the maximum static friction force F_f on these blocks, which are calculated under the assumption that the static friction coefficient between the blocks and the sand core is 0.6. It should be noted that we focused only on the case of the landward slope of 1/2 because the value of F_t was larger than that of F_f before the impingement of the tsunami for the landward slope of 1/1.

As indicated in Figure 10, the value of F_t increases and simultaneously that of F_f decreases at the impingement of the tsunami regardless of the location of the blocks. This results in small difference between F_t and F_f approximately from t = 42.5 s to t = 47.5 s. Furthermore, a comparison between Figure 10(a) and 10(b) indicates that this difference is very small for the block below the berm (S_m) compared with that between the berm and the toe (S_o). As a result, it is suggested that the block below the berm would be more vulnerable against the tsunami overflow.

CONCLUSIONS

Tsunami overflow on a coastal dike and resulting local scouring at its landward toe were investigated using a three-dimensional coupled fluid-structure-sediment-seabed interaction model (FS3M; Nakamura and Mizutani, 2014) and its verification hydraulic experiments. The main conclusions of this study are as follows:

1. From a comparison with experimental data, the predictive capability of the FS3M was demonstrated in terms of water surface fluctuation and the profile of a scour hole at the landward toe of the dike after the tsunami overflow.
2. An increase in pore-air pressure inside the dike caused seaward and upward force on armor blocks at the seaward side, upward force at the crown and the berm, and landward and upward force at the landward side.
3. At the landward slope of the dike, armor blocks below the crown and the berm received large landward and upward force because of the increase in the pore-air pressure and a decrease in water pressure induced by the flow separation. This suggested that these blocks would be vulnerable against the tsunami overflow.

ACKNOWLEDGEMENTS

This research was supported by the Ministry of Land, Infrastructure, Transport and Truism of Japan under the Research and Development of River and Sediment Control Technology (Coastal Technology Field).

REFERENCES

Bear, J. (1972). *Dynamics of Fluids in Porous Media*. American Elsevier Pub. Co., New York, 764 p.

Chock, G., Robertson, I., Kriebel, D., Francis, M., and Nistor, I. (2013). *Tohoku, Japan, Earthquake and Tsunami of March 11, 2011: Performance of Structures under Tsunami Loads*, ASCE, 330 p.

Hatogai, S., Suwa, Y., and Kato, F. (2012). “Hydraulic model experiments on scour landward of the coastal dike induced by tsunami overflow.” *Journal of JSCE, Series B2 (Coastal Engineering)*, 68, 406-410 (in Japanese).

Kajishima, T. and Takiguchi, S. (2002). “Interaction between particle clusters and particle-induced turbulence.” *International Journal of Heat and Fluid Flow*, 23, 639-646.

Kotake, Y. and Isobe, M. (2012). “Experimental study on pressure distribution along landward slope of coastal dike due to tsunami overflow.” *Journal of JSCE, Series B2 (Coastal Engineering)*, 68, 891-895 (in Japanese).

Kunugi, T. (2000). “MARS for multiphase calculation.” *Computational Fluid Dynamics Journal*, 9(1), 1-10.

Mizutani, N., McDougal, W. G., and Mostafa, A. M. (1996). “BEM-FEM combined analysis of nonlinear interaction between wave and submerged breakwater.” *Proc., 25th International Conference on Coastal Engineering*, ASCE, 2377-2390.

Nakamura, T. and Mizutani, N. (2014). “Development of fluid-sediment-seabed interaction model and its application.” *Proc., 34th International Conference on Coastal Engineering*, ASCE, 34, sediment.85, E93.

Nakamura, T. and Yim, S. C. (2011). “A nonlinear three-dimensional coupled fluid-sediment interaction model for large seabed deformation.” *Journal of Offshore Mechanics and Arctic Engineering*, ASME, 133(3), 031103-1-031103-14.

Nakao, H., Sato, S., and Yeh, H. (2012). “Laboratory study on destruction mechanisms of coastal dyke due to overflowing tsunami.” *Journal of JSCE, Series B2 (Coastal Engineering)*, 68, 281-285 (in Japanese).

Numerical Simulation on Scour behind Seawalls Due to Tsunami Overflow

Dong Wang[1]; Taro Arikawa[2]; Shaowu Li[3]; and Hayao Gen[4]

[1]State Key Laboratory of Hydraulic Engineering Simulation and Safety, Tianjin Univ. Tianjin 300072, China. E-mail: Wdong@tju.edu.cn
[2]Port and Airport Research Institute, 3-1-1, Nagase, Yokosuka, Japan 239-0826, Japan. E-mail: arikawa@pari.go.jp
[3]State Key Laboratory of Hydraulic Engineering Simulation and Safety, Tianjin Univ. Tianjin 300072, China. E-mail: lishaowu@tju.edu.cn
[4]Praia Consultant Co. Ltd, 3-5-7, Kawazaki, Japan 213-0011, Japan. E-mail: hayao@praia.co.jp

ABSTRACT

During the Great East Japan Earthquake of March 11, 2011, many protective structures were damaged by tsunami overflow. Some previous results of researches indicate the declining of the safety factor of bearing capacity due to scouring near the foundation of structures. However, the relation between scouring depth and overflow parameters has not yet been well understood. In this study, the scouring depth due to tsunami overflow is investigated by using numerical model based on SPH method and the numerical results are compared with those of the physical model tests. The analysis of numerical results concludes that the maximum depth of scouring is proportional to the height of overflow and is inversely proportional to the falling height of the overflow over the dike.

INTRODUCTION

Since the Great East Japan Earthquake, researchers have been paying more and more attention on the erosion mechanism for the protective structures under tsunami overflow (Sugano et al., 2014; Takahashi et al., 2014; Nakamura and Mizutani, 2014). According to the investigation (Arikawa et al., 2014), scouring on the back side of the dike by continuous tsunami overflow will seriously reduce the stability of the structure, which has not yet been paid much attention in the previous researches. Noguchi et al. (1997) has studied the scouring in front of a revetment under a solitary wave and demonstrates that the scoring is caused by a return flow. According to their results, the depth of scouring is proportional to the eddy scale generated by the return flow. Since a solitary wave lasts only for a short period, it is difficult to clarify whether his explaination is applicable to the prolonged overflow of tsunami.

The purpose of this research is to study the inherent relationship between the depth of scouring behind the seawall and its main factors of influence by using numerical simulation and experiment data.

EXPERIMENT

Scouring tests behind a vertical dike were conducted by Arikawa et al. (2014) in a flume sized with 105m in length and 0.8m in width and the model scale of 1/42. A rectangular wooden box with a crest width of 49cm was placed in the flume as a model of vertical dike (Fig.1). The sand with mediate grain size of 0.21mm was filled in the back of the vertical dike as erosion material. The height from the ground surface of the filled sand to the top of the sea dike was set as 24cm, 34cm and 48cm, respectively. Two submerged pumps with the same capacity were installed at the inflow end of the flume to maintain the continuous and constant flow discharge.

An overflow weir was placed in the flume to work as the vertical dike with the height being adjustable. The experiment conditions of the tests are shown in Table 1, the parameters of which are illustrated in Figure 1.

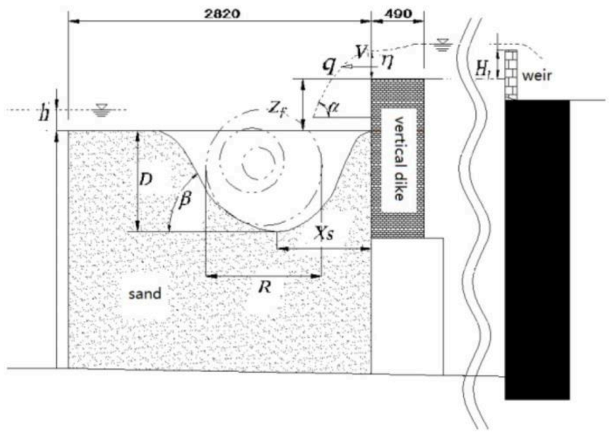

Figure 1. Cross section view of the test

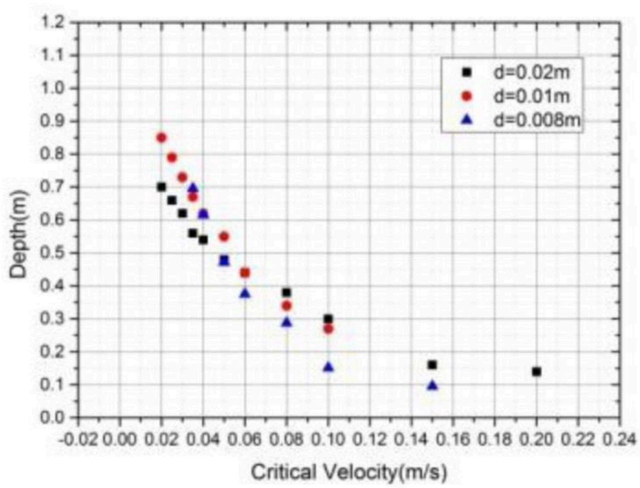

Figure 2. Sensitivity analysis of critical velocity

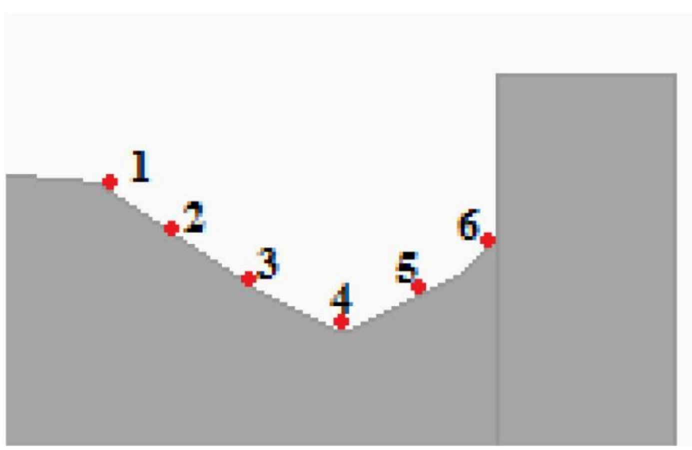

Figure 3. Topography of CADMAS model

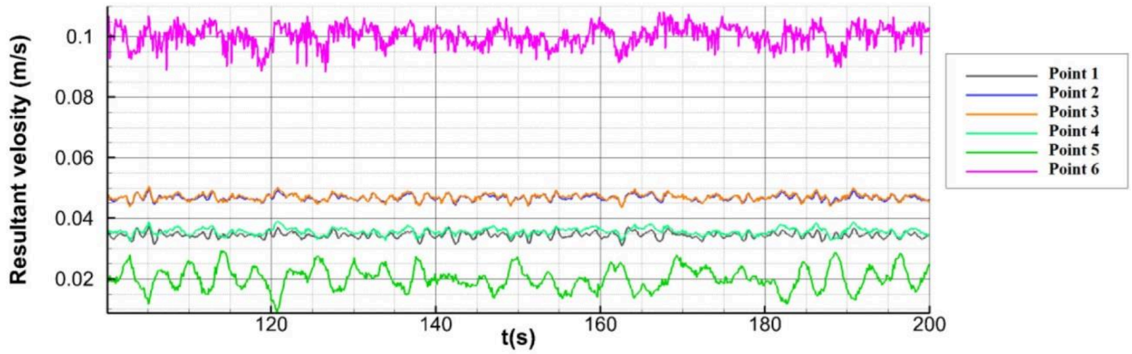

Figure 4. Comparison velocity at 6 measuring points

Table 1. Experiment conditions of the tests

Case	z_f (cm)	H_1 (cm)	η (cm)	h (cm)	v (m/s)	q (m^3/sm)
1	24	-13.2	1.0	0	0.17	0.002
2		-8	3.3	2.5	0.80	0.026
3		0	4.7	5.5	1.09	0.051
4		5	6.0	8.6	1.31	0.078
5		16	6.8	13.9	1.37	0.093
Case	z_f (cm)	H_1 (cm)	η (cm)	h (cm)	v (m/s)	q (m^3/sm)
6	34	0	4.2	5.1	1.06	0.045
7	48	0	4.0	5.4	1.07	0.043
8		0	4.2	5.5	1.09	0.046

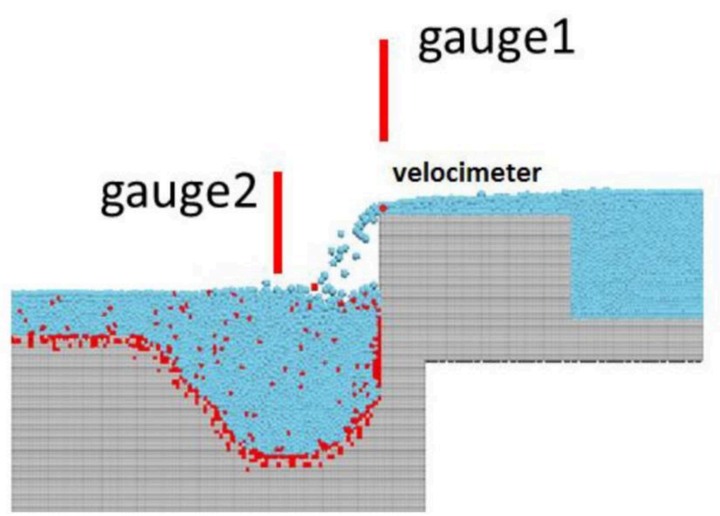

Figure 5 Location of the two gauges and the velocimeter

By following Noguchi et al. (1997), scouring related quantities are defined as follows: z_f the height from the initial ground surface of the filled sediment material to the crest of the vertical dike; η the overflow depth at the crest of the vertical dike (inlet side); v the flow velocity at the crest of the vertical dike; q the flux of falling water; D the maximum scouring depth; X_s the horizontal distance from the position of the maximum depth of the scouring pit to the vertical